RESEARCH

Sol-Gel/Gel Casting Nanoarchitectonics of Hybrid Fe_2O_3–ZnO/PS-PEG Nanocomposites and Their Optomagnetic Properties

Ali B. Abou Hammad[1] · A. M. Mansour[1] · Thoraya Maamoun Elhelali[2] · Amany M. El Nahrawy[1]

Abstract

Polymer networks incorporated with iron and zinc oxide nanoparticles have superparamagnetic and electrical characteristics where it can be employed in a variety of significant applications. To achieve optimal distribution and connection of nanoparticles in various polymeric matrices, it is required to investigate their dispersion performance with varied contents and the impact on their physical characteristics. A controlled sol-gel method is used combined with gel casting to synthesize organic-inorganic nanocomposites of $(ZnO)_x(1-x)Fe_2O_3$ loaded within a polystyrene-polyethylene glycol matrix. The structural and morphological assembly of the hydrogen bonds between the inorganic and organic parts is verified using X-ray diffraction (XRD) and scanning/transmission electron microscope (SEM/TEM) for the synthesized nanocomposites. The existence of the Fe aggregates, Zn/Fe pairs, and organic molecules was also confirmed by FTIR spectra. Optical and magnetic properties were evaluated. The band gap, refractive index, optical dielectric constant, and optical electronegativity were extracted.

Keywords ZnO · PS · PEG · Fe_2O_3 · Nanocomposites · Sol-gel · Optomagnetic

1 Introduction

Recently, applications posed strong desires for materials, which are relatively more difficult to meet using single-component structures and equable to a single class of materials, like only organic or only inorganic materials. In hybrid matrices, organic and inorganic constituents are repeatedly integrated through the same assembly that yields organic-inorganic hybrid systems that combine the auspicious properties of both types of structure blocks as evinced [1–3].

Polystyrene is a hard, rigid thermoplastic with a high refractive index, low thermal conductivity, transparent to visible wavelengths, low softening temperature, good electrical insulation, ease of processability, low moisture absorption, good dimensional precision, clarity, and low cost [4]. To enhance the properties of PS for specific applications, the PS is blended with some other polymers or molecules [5].

Polyethylene glycol (PEG) is a polyether composed of ethoxy units produced from the polymerization of ethylene oxide. Because it is a linear polymer with chemically active hydroxyl groups at both ends, conjugation with functional groups in a PE gylation process allows nanoparticles (NP) to be coupled to a linear chain through functional groups [6]. Due to its properties, such as electrical neutrality, considerable spatial repulsion, and high hydrophilicity, PEG is often chosen as one of the shielding groups for adsorption or grafting applications on the surfaces of NPs [7]. The PE gylation process can occur in three forms [7]: first, through physical adsorption, such as electrostatic or hydrophobic contact, PEG can physically attach to NPs, secondly, a strong chemical bond can be formed and it can be safely grafted onto the surface of NPs, third, it may combine with hydrophobic molecules to create macromolecules that can self-assemble into PE gylated NP in solution by joining with other molecules or themselves.

Metal oxide nanoparticles can improve the quality of polymer composites due to their excellent thermal stability, chemical resistance, mechanical strength, optical, and antibacterial properties [4]. They have special qualities because of their tiny size and high surface area [8]. Applications for transition metal-doped systems include lasers, photocatalysts, sensors, and ceramics [9]. The idea of coupling a metal oxide

✉ A. M. Mansour
amamansour@gmail.com; ae.mansour@nrc.sci.eg

1   Physics Research Institute, National Research Centre, 33 El-Bohouth St., Dokki, Giza 12622, Egypt

2   Department of Physics, Science College, Jazan University, Jazan, Saudi Arabia

with a polymer system was introduced to develop a system that could support the metal oxide for better activity. Such an immobilized system with polymer-supported inorganic NPs finds application in optoelectronics, sensors, photocatalytic, water purification, and others. Due to their stunning electrical, magnetic, and optical capabilities, which have drawn greater attention from scientists working on new technologies and materials, Fe and Zn are good candidates to change a variety of polymeric systems [10]. Recently, coupling zinc nanoparticles ZnO NPs within Fe_2O_3 magnetic system is an attractive approach that has been explored. The recyclability of these structures supports the formation of a vast band gap, higher transparency systems, and excellent audio features, owing to electronic chattels, higher electron mobility, and environmental affability [11, 12]. Therefore, In this study, work on PS:PEG polyblend has been taken as an active area for research having developed properties to be employed for further investigation. Interestingly the substitution of Fe ion with Zn ion into the PS-PEG/Fe matrix has a significant effect on structural, optical, and magnetic properties. The polymer networks that contain integrated iron and zinc oxide nanoparticles exhibit superparamagnetic and electrical properties features. Due to these benefits, nanocomposites are employed in several important applications, such as drug delivery process, cell separation, cancer hyperthermy, magnetic resonance imaging, tissue fast healing, and detectors [10].

Herein, mixing PS with polyethylene glycol allows Fe_2O_3/ZnO more dispersion, increasing the ionic conductivity and chemical stability of PS/PEG/Fe–Zn complexes owing to the partial crystallinity of both polymeric and Fe–Zn nanoparticles [13, 14]. Direct assembly of the sol-gel and the gel casting methods to fabricate PS-PEG loaded with Fe_2O_3 and Fe_2O_3/ZnO is attractive since it is appropriate to use a wide range of various nanosized particles. It also expressively simplifies the formation procedures of nanocomposites, progresses their performance, and enhances multifunctionality, and repeatability. This work aims to modify polystyrene-PEG-based composites and improve their impact by introducing Fe_2O_3 and Fe_2O_3 doped with ZnO NPs. Investigation of the structural, optical, and magnetic properties of the PS-PEG polymer blend doped with $(1 − x)Fe_2O_3(ZnO)_x$, (x = 0–7 mol%), formed using sol-gel and gel casting methods were done to demonstrate their use in optomagnetic and optoelectronic technologies.

2 Experimental Details

2.1 Materials

Polystyrene (PS) used in this study was purchased from Heliopolis Company for Chemical Industries. Ferric nitrate $(Fe(NO_3)_3 \cdot 9H_2O, 99.99\%)$, and Zinc acetate $((CH_3CO_2)_2Zn,$ 99.99%) were purchased from Sigma-Aldrich. The acquired solvents (i.e., methanol (MeOH) and toluene $(C_6H_5CH_3)$) were bought from Sigma Aldrich (USA). All these chemicals were employed as extradited.

2.2 Preparation of PS-PEG-Fe$_2$O$_3$/ ZnO Nanocomposites

The sol-gel liquid solution of Fe_2O_3 with different concentrations of ZnO nanoparticles was prepared by dissolving the stoichiometric amounts of Fe_2O_3 and ZnO, hydrochloric acid (HCL), and H_2O, from ferric nitrate $(Fe(NO_3)_3 \cdot 9H_2O)$ and zinc acetate $((CH_3CO_2)_2Zn)$ as a raw source for ZnO/Fe_2O_3, which is stressed with further details previously [15–17].

The solution of Zn/Fe was stirred for 30 min at room temperature to get a homogeneous brownish solution called Sol A. Polystyrene-PEG-ZnO doped with Fe^{3+} nanocomposite and was prepared using the solution casting route. In this route, 6 gm of polystyrene dissolved in toluene under strong stirring, then sonicated for 20 min and blended with PEG dissolved in 60 ml distilled water. After this, the liquid polymeric phase of $PS-PEG-Fe_2O_3$ doped with (0–7 mol%) ZnO has been mixed under stirring for 70 min at 40 °C to obtain a homogenous nanocomposite. Finally, the formed nanocomposites were cast in Petri dishes and aged until dried. The preparation steps were sketched in Fig. 1.

2.3 Characterization Methods

The resulting nanocomposites have been characterized by X-ray diffraction of prepared nanocomposite films have been obtained by using Bruker- D8 focus X-ray-Diffractometer, Germany equipped with CuKα (λ = 1.54 nm) at (40 KV) and (40 mA) in the (2θ) range of 5°–75°. The uncertainty of the XRD phase analysis utilizing Rietveld refinement falls generally within a range of 1–3%. The presence of different phases has been specified by using JCPDS data files in Pcpdfwin-software. The particle size of the film samples was examined by HR-TEM (JEM-2100) Joel, Japan. Fourier transform infrared (FTIR) spectra of formed films have been registered by using Perkin-Elmer (C92035) with uncertainty in the order of 0.05%. Absorption spectra have been obtained from 1300 to 400 cm^{-1}.

The optical spectra of the prepared nanocomposites were measured by a Jasco V-570 spectrophotometer (with wavelength and photometric accuracy of ± 0.2 nm and ± 0.002 Abs, respectively) over the wavelength range, of 0.2–2.5 μm. Magnetic measurements were done at Room temperature and carried out under the application of a magnetic field up to ± 15 kOe using a Lakeshore(7404) vibrating sample magnetometer (VSM) (uncertainty of only ~2%).

Fig. 1 The preparation steps of PS-PEG-Fe$_2$O$_3$/ZnO nanocomposites
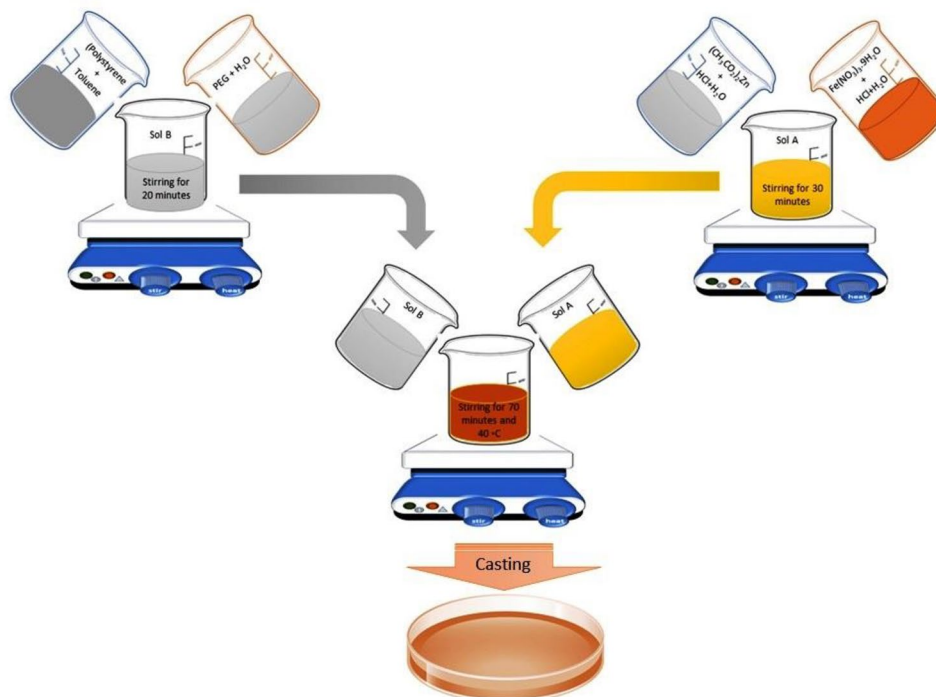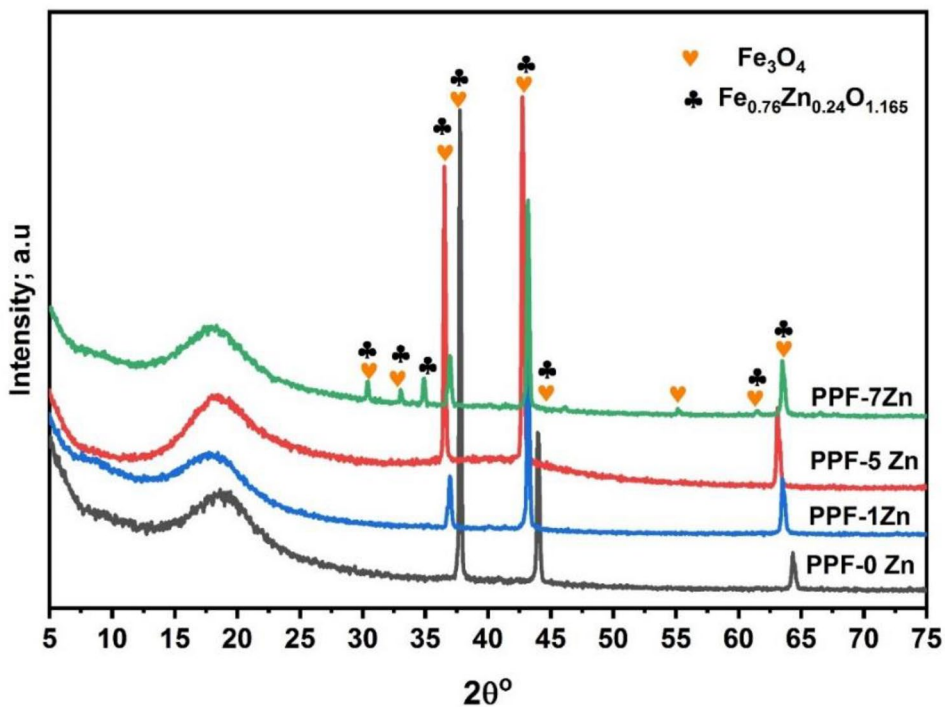

Fig. 2 The XRD patterns of PS-PEG-Fe/(0–7)ZnO nanocomposites

3 Results and Discussion

3.1 XRD Analysis

The XRD patterns give the structural results of PS-PEG-Fe$_2$O$_3$/(0–7)ZnO nanomembranes were displayed in Fig. 2. XRD spectra appeared that the used compositional of pure and doped PS, PEG, Fe^{3+}, and ZnO, gave evidence of the successful formation of within the blended PS-PEG polymeric matrix with characteristic broad XRD peaks at

$2\theta = 8.92°$ and $18.23°$ linked to PS-PEG-Fe_2O_3 matrix (03-0347) [4, 9, 10, 18].

The XRD pattern of the pure sample has two phases with the main three peaks at $2\theta = 37.7°$, $43.95°$, and $64.32°$, as represented in Fig. 2. These peaks are related to Fe_3O_4 phase formed in PS-PEG-based according to ICDD card No: 03-065-3107. With the introduction of ZnO nanoparticles, all XRD peaks are shifted to lower (2θ), this resulted from the inner reaction between Fe and Zn leads to the zinc ferrite phase corresponding to $Fe_{0.76}Zn_{0.24}O_{1.165}$ (ICDD card No: 00-048-0567 of iron zinc oxide). Also, with the higher ZnO ratio, new peaks appeared at $2\theta = 30°–33.57°$, attributed to zinc ferrite oxide within the blended PS-PEG matrix, which can be a precise indicator of the PS-PEG-Fe-Zn nanocomposite forming ability at a lower temperature [19].

The sharp and strong XRD peaks of the formed nanocomposites indicate the respectable crystalline nature of nanoparticles [1, 20]. The change in XRD peak intensities within the 2θ range $29°–65°$ and the differences in some XRD peak intensities were mainly attributable to the change in Fe_2O_3 levels in the PS-PEG-based with increasing ZnO ratio. According to Debye-Scherrer's equation [21], the three predominant XRD peaks at $2\theta = 36.53°$, $37.76°$, and $44°$ are used to evaluate the crystallite size. The evaluated crystallite size increases from ~ 17 nm (PS-PEG-Fe_2O_3) up to ~ 20.79 nm (PS-PEG-Fe_2O_3/ZnO).

3.2 SEM/TEM Study

The SEM micrographs of PPFe and PPFe doped with 7 ZnO magnetic nanocomposites are given in Fig. 3a, b. It can be observed that the nanocomposites have a flat and dense surface with some nanospheres shape on their surface for the 7 Fe^{3+} samples (Fig. 3a). The Fe-doped nanocomposite shows a smooth surface and has good dispersion (Fig. 2b). The TEM micrograph and particle distribution appear the uniformly distributed gray and dark dots with spherical shapes in the nano-sizes range can be observed in Fig. 3c–e, which denotes that Fe_2O_3 and $Fe_{0.76}Zn_{0.24}O_{1.165}$ that were successfully formed and dispersed in the PS-PEG matrix. The average particle size (Fig. 3d) is nearly 23 nm.

There is a continuous crystalline development for Fe-ZnO nanoparticles within the PP matrix, which stabilizes the polystyrene network. Herein, polyethylene glycol and solvents were utilized as a supporter and stabilizer for PS-PEG/ Fe_2O_3/ZnO nanocomposites [22]. Hence, SEM and TEM results support the formation of appropriate Zn/Fe-containing forming controllable nano-metal-organic complexes.

3.3 Infra-red Spectroscopy

Infrared spectroscopy is studied to portray the synthesis of the Zn/Fe nanoparticles through sol-gel processes (hydrolysis and condensation) together with the expansion of the Polystyrene-polyethylene organic network during the synthesis and aging processes [4, 23, 24]. Evidence of the chemical structure of the PPFe and Zn doped nanocomposites, FTIR was used to allocate the altered characteristic absorption groups. Figure 4 gives the full FTIR range spectra of PPFe and PPFe doped with 3, 7 ZnO magnetic nanocomposites. At a larger wavenumber, bands connected with OH (around 3450 cm^{-1}), CH and OH (2849 up to 3125 cm^{-1}), and CH_3 (2856 cm^{-1}) vibrations were perceived [25, 26].

In the mid-IR region, the organic polymerization is evidenced by the links of PS-PEG and increases the intensity at $1449–1599$ cm^{-1} with increasing Zn contents. Zn/Fe polymerization is represented by the $1023–533$ cm^{-1} range of the FTIR spectra. Doping PPFe nanocomposite with ZnO nanoparticles has been established to enhance their structural and chemical benefits, and the polymeric crystallization degrees [27–29].

The absorption bands at 533 cm^{-1}, 679 cm^{-1}, 753 cm^{-1}, and 1023 cm^{-1} in the spectra of the undoped and Zn doped samples, are attributed to the Fe–O–Fe and Fe–O–Zn and –CH_3 rocking mode of Fe–O–CH_3 [30].

The change in the peaks intensity in the range 533 cm^{-1} to 1023 cm^{-1} supports the good formation and that the combination of polyethylene glycol (PEG) polystyrene (PS) helps Fe_2O_3 and Zn/Fe nanoparticles to overcome the accumulation between the magnetic nanoparticles.

This is evidence of condensation reactions between Fe_2O_3, ZnO, and –OH groups before being mixed with the PS-PEG matrix that results from the sol-gel/gel casting treatment of the prepared samples.

3.4 Optical Analysis

The optical characteristics rely on a variety of factors, including doping, surface morphology, preparation method, preparative parameters, and interactions with their surroundings [31, 32]. The studies of the absorption coefficient of semiconducting materials give important data about the electronic states in the high energy part of the optical absorption range, while the other lower energy part of the spectrum agrees with the atomic vibrations [4, 33, 34].

Figure 5a shows the optical transmission and reflection of PS-PEG/(Zn doped FeO) films in the wavelength range of 200–2500 nm. The nanocomposite films showed an increase in optical transmittance to about 75% with increasing of Zn. The transmittance increase with increasing Zn content in the loaded inorganic materials is a reflection of changes in

Fig. 3 SEM images for **a** PPFe, **b** PPFe-7ZnO, **c**, **d** the TEM for PPFe-(3, 7) ZnO, and **e** the particle distribution of PPFe-(3) ZnO nanocomposites
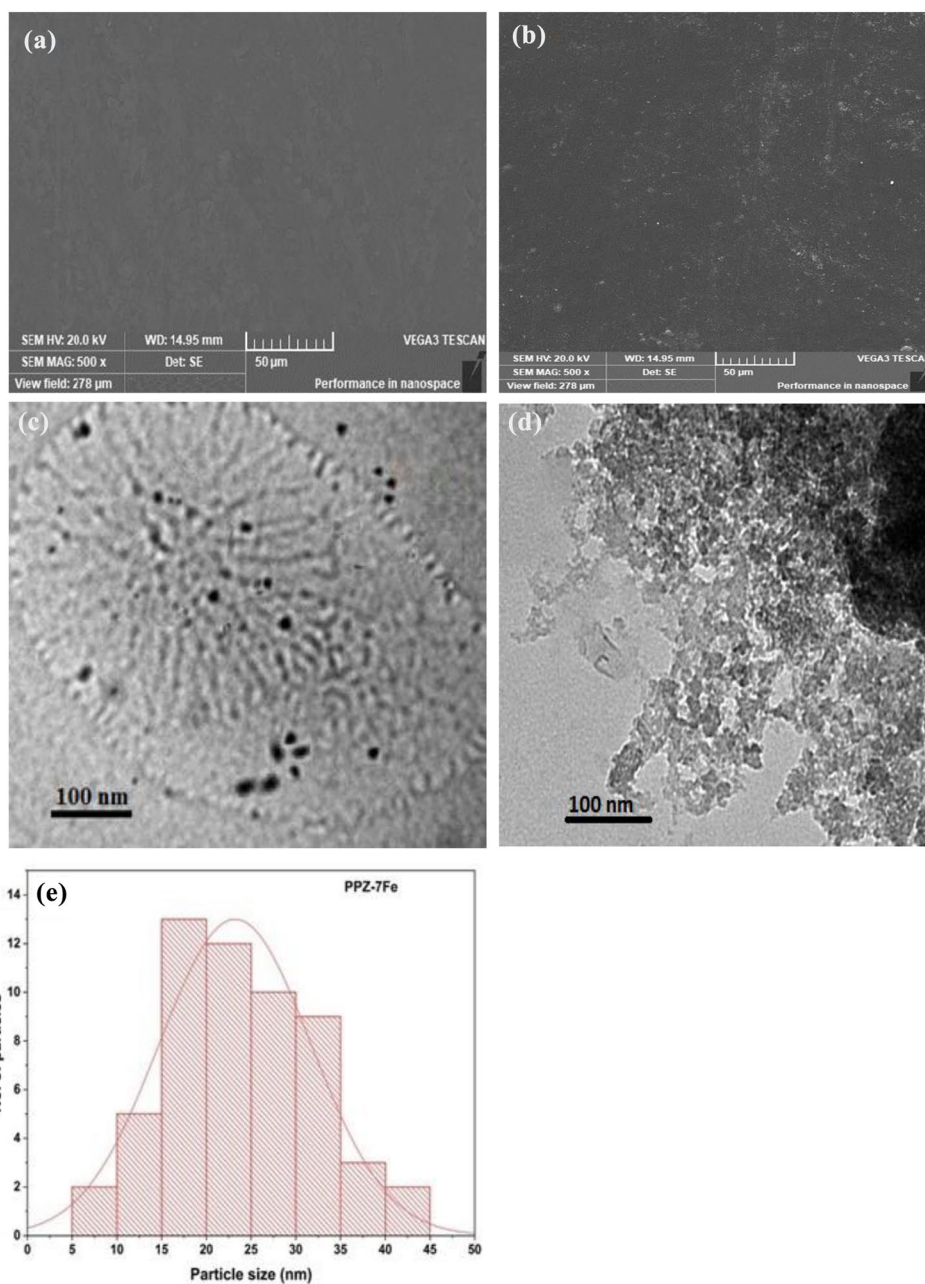
the crystalline quality and surface roughness of the films. This case is more significant in films with lower surface roughness which leads to less surface scattering of light [35]. Salaken et al. [36] reported that the decrease in Zn content in Fe-Zn nanocomposite led to similar results for Fe-doped ZnO films by varying the Fe doping concentration from 1 to 5 at%. They noticed less optical transmittance for Fe-doped films than pure ZnO films. Also, Srinivasulu et al. Al. [35] observed a behavior similar to that in Fe-doped ZnO prepared by spray pyrolysis at a substrate temperature of 400 °C. Here, the presence of interference peaks in the transmittance spectra at higher wavelengths might be attributed to

the higher film thickness and larger grain size of the grown films [35] as found by X-ray analysis.

The dependence of the optical absorption coefficient of PS-PEG/(Zn doped FeO) films upon the incident wavelength for the different ratios of Zn-concentrations is depicted in Fig. 5b. It decreases with increasing the light wavelengths but slightly increases with the inorganic phase. Furthermore, at 216 nm, an absorption peak was observed. From the figure, one can observe that the fundamental absorption edge is shifted to a lower wavelength side as the dopant concentration increases. Since the absorption edge that corresponds to the electron transition from the valence to the conduction

Fig. 4 FTIR spectra for **a** PPFe, **b** PPFe-3ZnO, and **c** PPFe-7ZnO nanocomposites
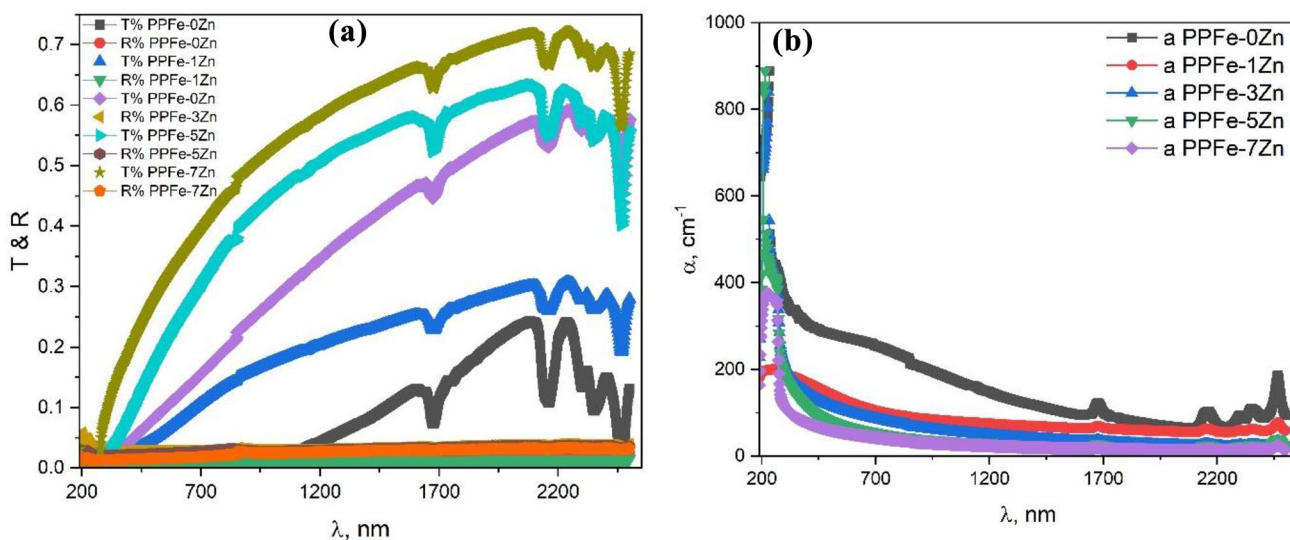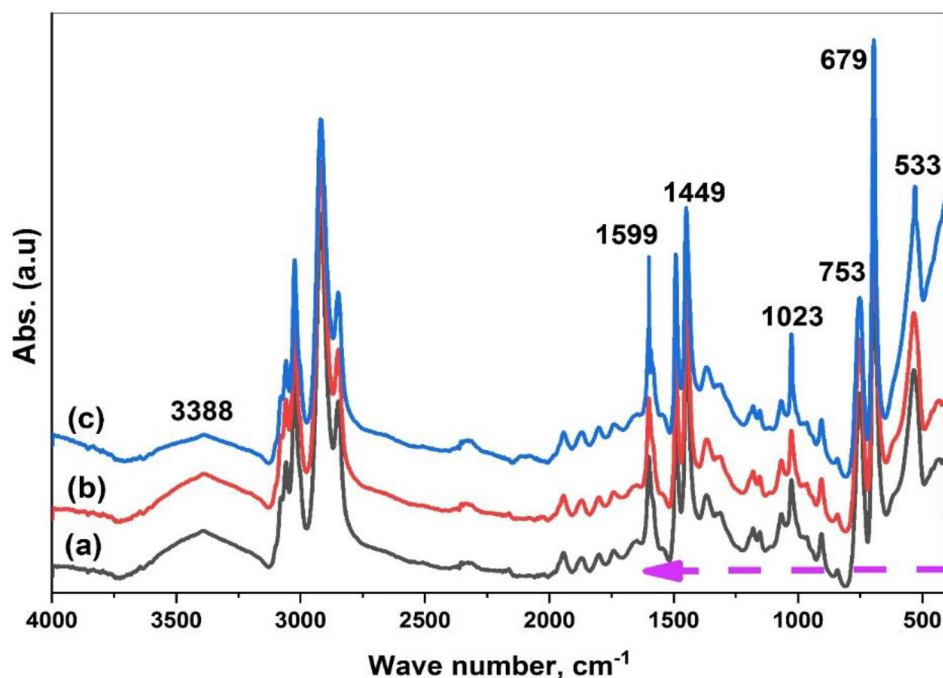

Fig. 5 **a** Transmission and reflection, **b** absorbance coefficient of the PPFe-(0–7)ZnO nanocomposites

band was used to calculate the absorption coefficient (α), the optical band gap of the PS-PEG/(Zm doped FeO) films can be determined by applying the Tauc relation [37]:

$$\alpha h\nu = Q(h\nu - E_g)^{\frac{1}{2}},$$

where Q is a constant, $h\nu$ is the photon energy, and E_g is the optical band gap of the material.

The plots of $(\alpha h\nu)^2$ versus $(h\nu)$ showed straight lines in the higher energy domain as shown in Fig. 6a, where it represents an indirect allowed transition. The energy band gap (E_g) of the films can be determined by extrapolating the linear part of the straight lines onto the energy axis to reach $(\alpha h\nu) = 0$.

The evaluated band gaps are 1.246, 2.032, 2.619, 2.969, and 3.427 eV for 0, 1, 3, 5, and 7 wt% Zn, respectively. By the addition of FeO doped by 0, 1, 3, 5, and 7 wt% Zn, the band gap increases to higher values as shown in Fig. 6b. These findings demonstrated that the optical band gap energy was directly associated with the content of an

Fig. 6 **a** The plots of $(\alpha h\nu)^2$ versus $(h\nu)$, **b** The band gap behavior with Zn content, **c** The plot of $(\ln\alpha)$ versus $(h\nu)$, **d** the change of Urbach energy with Zn content, and **e** The extinction coefficient behavior with increasing wavelength for the PPFe-(0–7)ZnO nanocomposites
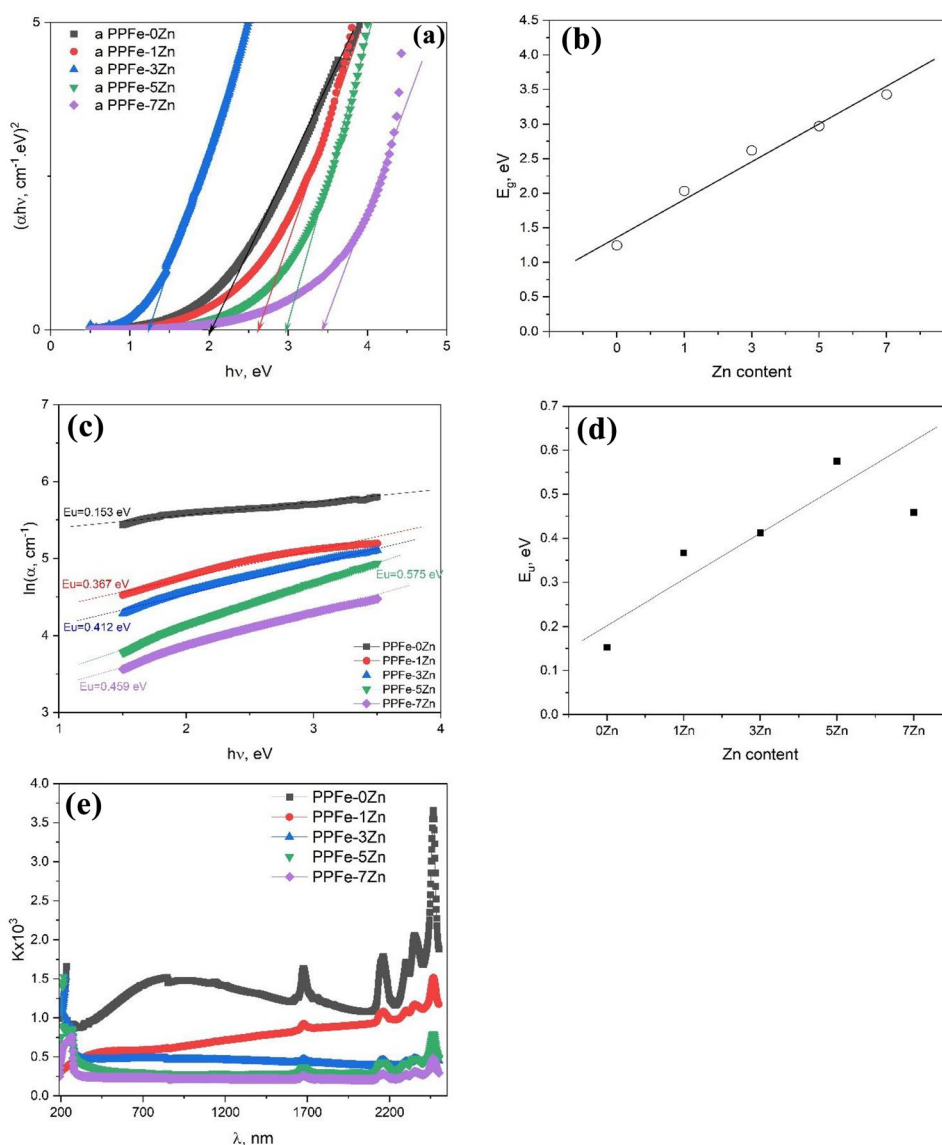
improvement in carrier-carrier interaction that caused a shift in the transition band [38]. The Zn^{2+} ions are substituted into Fe^{3+} ionic sites, then they can prevent additional free carriers which lead to an increase of energy needed for band gap transition [35, 39]. The decrease of the ion transport between the polyblend and inorganic phase may be responsible for the decrease in band gap energy [2].

The spectrum dependence of the absorption edge is thought to follow the empirical Urbach rule in the low photon energy band. This energy is frequently used to refer to the length of the bandgap's tail of localized states. Because disordered and amorphous materials produce localized states that are stretched in the bandgap, the exponential tail is observed. The Urbach energy (E_u) can be used to gauge a material's level of disorder, contaminants, and flaws [15]. This characteristic is related to the localized state of the conduction band and the prolonged

transition of the valence band. The Eu value was determined for each sample using the formula shown in [15]:

$$\alpha = \alpha_0 \exp\left(h\nu/E_u\right)$$

where $h\nu$ is the photon energy, Eu is the Urbach energy, and α_0 is a constant. By plotting $(\ln\alpha)$ versus $(h\nu)$, as shown in Fig. 6c, the E_u values can be extracted as 0.153, 0.367, 0.412, 0.575, and 0.459 eV for polyblend loaded by FeO doped by 0, 1, 3, 5, and 7 wt% Zn, respectively. These substantially lower E_u values show that the prepared samples have high disorders or flaws, and they also represent the decreased density of localized states in their structures. Furthermore, the E_u increase with the inorganic phase loading, and with the Zn content increase as in Fig. 6d. This suggests that with the loading of polyblends by an inorganic phase, the grade of disorder and flaws increase.
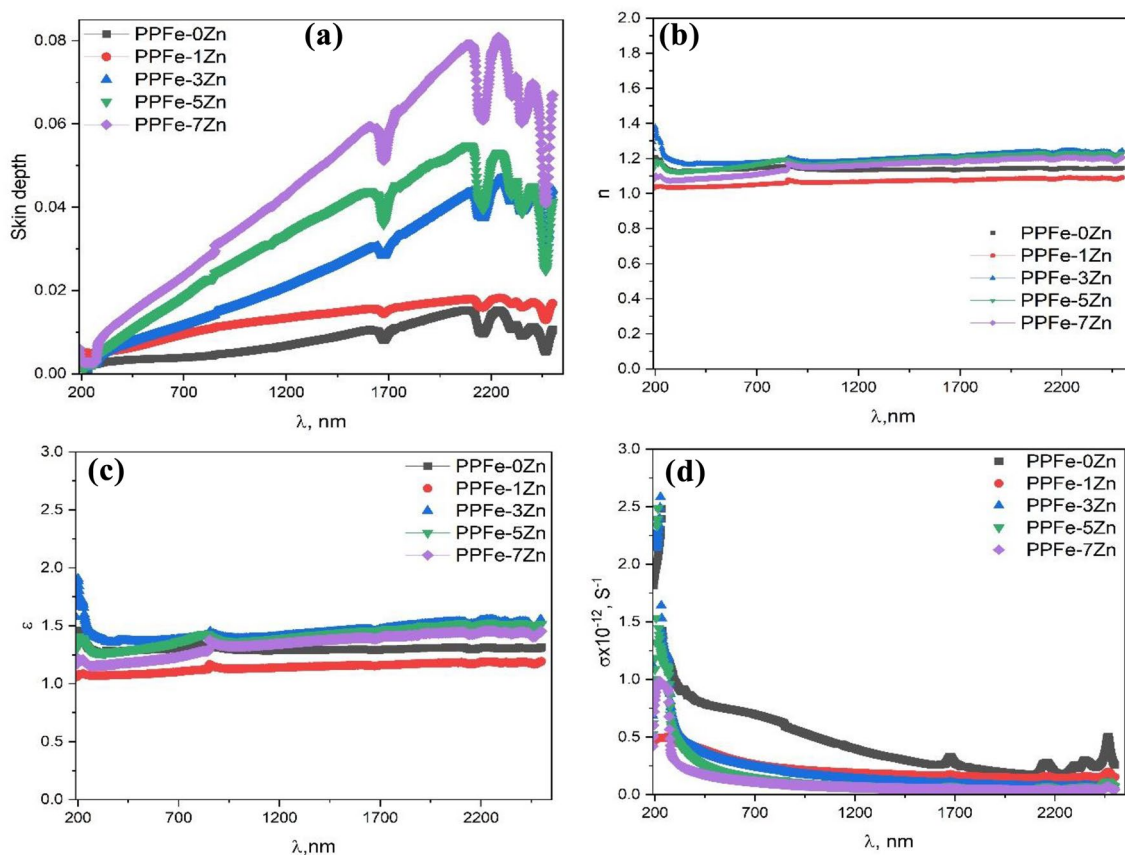
Fig. 7 **a** The depth of the skin, **b** The refractive index, **c** The dielectric permittivity, and **d** The optical conductivity behavior with wavelength for the PPFe-(0–7)ZnO nanocomposites

The extinction coefficient (*k*) is calculated by [40]:

$$k = \alpha \lambda / 4\pi$$

The extinction coefficients decrease with the loading of FeO doped by Zn with different content as shown in Fig. 6e. It increases very slightly with increasing wavelength due to the decrease of incident photon energy near the surface [41].

The penetration depth or skin depth (δ) is known as an incident photon flux decrease as light passes through the material [40]. δ is calculated by [40]:

$$\delta = 1/\alpha$$

The behavior of the depth of the skin with wavelength change is presented in Fig. 7a. The δ increase with the addition of the Zn. With increasing in wavelength, the skin depth increases.

Figure 7b represents the dependence of the refractive index on the change in wavelength for the prepared samples. The n values increase slightly with an increase in wavelength and take the value between 1 and 1.2 for all samples.

The ability of a solid to interact with an electric field or an electromagnetic field is indicated by its dielectric permittivity [40]. As it depends on the refractive index values, the dielectric permittivity takes the same behavior of it. As in Fig. 7c, the dielectric permittivity slightly increases with the increase in wavelength.

The change in optical conductivity (σ_{op}) change with the change in wavelength was plotted in Fig. 7d for the prepared samples along with the next Eqs. [26, 42]:

$$\sigma_{opt} = \alpha nc / 4\pi$$

where α, n, and c, respectively are the absorption coefficient, refractive index, and speed of light. The σ_{op} *nearly* decreased as the wavelength increased. With increasing Zn content, the optical conductivity is slightly decreased.

3.5 Magnetic Properties

The magnetic properties of PPFe-Zn were examined by the magnetization curve (M vs. H) at room temperature, Fig. 8a. A diamagnetic behavior is observed in sample PPFe-7Zn, where the magnetization decreases with
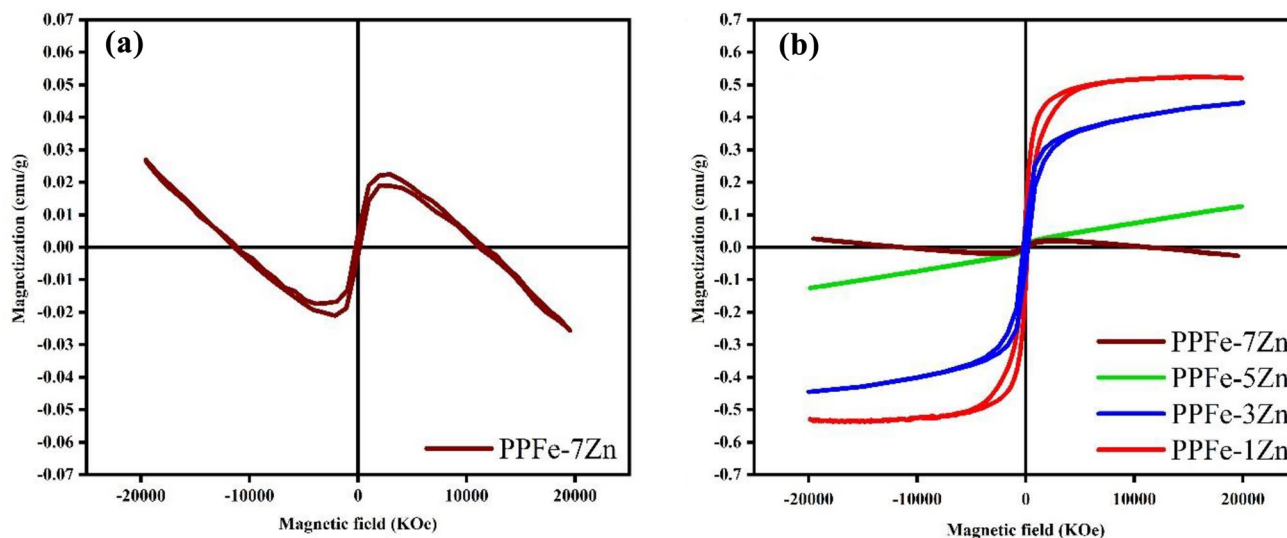
Fig. 8 The magnetic hysteresis loop (M vs. H) of PPFe-(0–7)ZnO nanocomposites at room temperature

Table 1 Magnetic parameters of PPFe-xZn, Magnetization (Ms), Remanence (M_r), and Coercive (Hc)

Sample	Ms (emu/g)	Mr (emu/g)	Hc (G)
PPFe-5Zn	0.1254	0.00613	185.74
PPFe-3Zn	0.445	0.0587	198.77
PPFe-1Zn	0.5312	0.10462	161.61

increasing the applied magnetic field at high field (a negative high-field slope). This behavior is attributed to the low concentration of the magnetic center in the sample (Fe^{3+}), and the diamagnetic polymer between the magnetic center resists the interaction between the magnetic centers. Therefore a diamagnetic behavior is observed in sample PPFe-7Zn [43–46].

According to Fig. 8b, a magnetic hysteresis loop is observed as the iron concentration increase. This observation can be interpreted as; the iron ions representing magnetic centers in the sample, therefore increasing the iron concentration increases the magnetic center concentration and the interaction power between them [47, 48]. Consequently, a magnetic hysteresis loop is observed under the effect of the external magnetic field. The presence of Fe monomers in the PS matrix promotes the magnetic state to support their magnetic properties. The magnetization of the nanocomposite changed with varying Zn concentrations, and the obtained results matched with those reported by Li et al. [49].

Table 1 presented the different magnetic parameters obtained from the hysteresis loop. The magnetization (M_s) and the remanence (M_r) increase with increasing the iron concentration. These data reflect the effect of iron on the diamagnetic polystyrene.

4 Conclusion

PS/PEG blend loaded by Fe_2O_3 doped with ZnO with different concentrations (0, 1, 3, 5, and 7 wt%) nanoparticles were prepared using a sol-gel process and casting route under stirring for 2 h at 40 °C. The PP-Fe_2O_3/ZnO nanocomposite shows an excellent crystalline degree and well dispersion of Fe and ZnO/Fe nanoparticles through the polymeric matrix. The FTIR results demonstrate that introduce of Fe_2O_3 and Zn/Fe nanoparticles in the PS-PEG matrix works as a growth factor producing good organic-inorganic interface nanocomposites. The addition of both Fe_2O_3 and Zn/Fe_2O_3 nanoparticles in PS-PEG enhances their magnetic properties. higher contents of ZnO nanoparticles enhance the coercivity and saturation magnetization. The band gaps increase from 1.246 to 2.032, 2.619, 2.969, and 3.427 eV with the addition of ZnO from 0, to 1, 3, 5, and 7 wt%, respectively. The Urbach energy also increase from 0.153 to 0.367, 0.412, 0.575, and 0.459 eV for FeO doped by 0, 1, 3, 5, and 7 wt% Zn, respectively. The refractive index increases slightly with an increase in wavelength and takes the value between 1 and 1.2 for all nanocomposites. Hence, from the produced results, the introduction of magnetic Fe_2O_3 and a wide band gap ZnO in PS-PEG modifies the structural, optical, and magnetic properties of these nanocomposites and will be useful candidates for various optoelectronic and storage applications.

Declarations

Conflict of interest The author declares that they have no conflict of interest.

Research Involving Human Participants or Animals This article does not contain any studies with human participants or animals performed by any of the authors.

References

1. A.M. El-Nahrawy, A.I. Ali, A.B. Abou, Hammad, A.M. Youssef, Int. J. Biol. Macromol. **93**, 267 (2016)
2. M. Barala, B. Siwach, R. Sangwan, K. Yadav, D. Mohan, S. Sanghi, Mater. Today Proc. **54**, 697 (2022)
3. S. Dacrory, A.B. Abou Hammad, A.M. El Nahrawy, H. Abou-Yousef, S. Kamel, ECS J. Solid State Sci. Technol. **10**, 083004 (2021)
4. A.M. El Nahrawy, A.B.A. Hammad, A.M. Youssef, A.M. Mansour, A.M. Othman, Appl. Phys. A Mater. Sci. Process. **125**, 1–9 (2019)
5. A.A. Higazy, H. Afifi, A.H. Khafagy, M.A. El-Shahawy, A.M. Mansour, Ultrasonics **44**, e1439–e1445 (2006)
6. L. Shi, J. Zhang, M. Zhao, S. Tang, X. Cheng, W. Zhang, W. Li, X. Liu, H. Peng, Q. Wang, Nanoscale **13**, 10748 (2021)
7. A.A. D'souza, R. Shegokar, Expert Opin. Drug Deliv. **13**, 1257 (2016)
8. A.M. El Nahrawy, A.M. Mansour, and A. B. Abou Hammad, Silicon **14**, 1227 (2022)
9. A.M. El Nahrawy, A.B. Abou Hammad, A.M. Bakr, T.I. Shaheen, A.M. Mansour, Appl. Phys. A **126**, 654 (2020)
10. A.M. El Nahrawy, A.S. Montaser, A.M. Bakr, A.B. Abou, Hammad, A.M. Mansour, J. Mater. Sci. Mater. Electron. **32**, 28019 (2021)
11. O.D. Maynez-Navarro, M.A. Mendez-Rojas, D.X. Flores-Cervantes, J.L. Sanchez-Salas, Air Soil Water Res **13**, 117862212097095 (2020)
12. O. Długosz, K. Szostak, M. Krupiński, M. Banach, Int. J. Environ. Sci. Technol. **18**, 561 (2021)
13. R. Hashaikeh, H. Abushammala, Carbohydr. Polym. **83**, 1088 (2011)
14. L. Ranjta, C.P. Singh, N. Rai, Mater. Today Proc. **54**, 702 (2022)
15. A.M. El Nahrawy, A.B. Abou Hammad, A.M. Mansour, Arab. J. Sci. Eng. **46**, 5893 (2021)
16. A.M. El Nahrawy, A. Elzwawy, A.B. Abou Hammad, A.M. Mansour, Solid State Sci. **108**, 106454 (2020)
17. A.M. El Nahrawy, A.I. Ali, A.B. Abou, Hammad, A. Mbarek, Egypt. J. Chem. **61**, 1073 (2018)
18. C. Manfredi, C. De Rosa, G. Guerra, M. Rapacciuolo, F. Auriemma, P. Corradini, Macromol. Chem. Phys. **196**, 2795 (1995)
19. Y.A. Alibwaini, O.M. Hemeda, R. El-Shater, T. Sharshar, A.H. Ashour, A.W. Ajlouni, E.A. Arrasheed, A.M.A. Henaish, Opt. Mater. **111**, 110600 (2021)
20. A.B.A. Hammad, A.M. El Nahrawy, D.M. Atia, H.T. El-Madany, A.M. Mansour, Int. J. Mater. Eng. Innov. **12**, 18 (2021)
21. A.M. Mansour, A.B. Abou Hammad, A.M. El Nahrawy, Nano-Struct. Nano-Objects **25**, 100646 (2021)
22. A.S. Abdulhadi, G.A. Gouda, A.M. Hamed, M.A. Abu-Saied, M.A. El-Mottaleb, Bull. Pharm. Sci. Assiut **45**, 23 (2022)
23. A.M. El Nahrawy, H. Salah El-Deen, A.A. Soliman, W.M.M. Mosa, Egypt. J. Chem. **62**, 525 (2019)
24. A.M. El Nahrawy, B.A. Hemdan, A.B. Abou Hammad, A.M. Othman, A.M. Abouelnaga, A.M. Mansour, Silicon **13**, 2979–2991 (2020)
25. M.M. Borgohain, T. Joykumar, S.V. Bhat, Solid State Ion. **181**, 964 (2010)
26. A.M.E. Nahrawy, A.M. Bakr, A.B.A. Hammad, A.M. Mansour, Egypt. J. Chem. **64**, 7293 (2021)
27. N.A. Al-Tayyar, A.M. Youssef, R.R. Al-Hindi, Food Packag. Shelf Life **25**, 100523 (2020)
28. K. Okamoto, C.K. Luscombe, Polym. Chem. **2**, 2424 (2011)
29. S.S. Bulla, R.F. Bhajantri, C. Chavan, K. Sakthipandi, J. Polym. Res. **28**, 1–21 (2021)
30. A.M. ElNahrawy, A.M. Mansour, H.A. ElAttar, E.M.M. Sakr, A.A. Soliman, A.B.A. Hammad, J. Mater. Sci. Mater. Electron. **31**, 6224 (2020)
31. A.A.M. Farag, A.M. Mansour, A.H. Ammar, M.A. Rafea, Synth. Met. **161**, 2135 (2011)
32. A.A.M. Farag, A.M. Mansour, A.H. Ammar, M.A. Rafea, A.M. Farid, J. Alloys Compd. **513**, 404 (2012)
33. A.M. El Nahrawy, A.M. Mansour, A.B. Abou, Hammad, A.R. Wassel, Mater. Res. Express **6**, 016404 (2019)
34. A.M. Mansour, Silicon **11**, 1989 (2019)
35. T. Srinivasulu, K. Saritha, K.T.R. Reddy, Mod. Electron. Mater. **3**, 76 (2017)
36. S.M. Salaken, E. Farzana, J. Podder, J. Semicond. **34**, 073003 (2013)
37. A.M. ElNahrawy, A.B. AbouHammad, Int. J. PharmTech Res. **9**, 16 (2016)
38. H. El-Zahed, A. El-Korashy, M.A. Rahem, Vacuum **68**, 19 (2002)
39. Z.N. Kayani, N. Yaseen, S. Riaz, S. Naseem, Mater. Res. Express **5**, 36418 (2018)
40. A.M. El Nahrawy, B.A. Hemdan, A.M. Mansour, A. Elzwawy, A.B. AbouHammad, Silicon **14**, 6645–6660 (2021)
41. F. Hcini, S. Hcini, M.A. Wederni, B. Alzahrani, H. Al Robei, K. Khirouni, S. Zemni, M.L. Bouazizi, Phys. B Condens. Matter **624**, 413439 (2022)
42. A.B. Abou Hammad, A.M. Mansour, A.M. El Nahrawy, Phys. Scr. **96**, 125821 (2021)
43. A.M. Mansour, R.S. Ibrahim, A.A. Azab, J. Mater. Sci. Mater. Electron. **33**, 10251 (2022)

44. R.S. Ibrahim, A.A. Azab, A.M. Mansour, J. Mater. Sci. Mater. Electron. **32**, 19980 (2021)
45. A.M. Mansour, J. Met. Mater. Miner **30**, 1 (2020)
46. A.A. Azab, A.M. Mansour, G.M. Turky, Sci. Rep. **10**, 1–11 (2020)
47. A.M. El Nahrawy, B.A. Hemdan, A.B. Abou Hammad, A.M. Othman, A.M. Abouelnaga, A.M. Mansour, Silicon **13**, 2979 (2021)
48. A.M. El Nahrawy, A.M. Mansour, A. Elzwawy, A.B. Abou, B.A. Hemdan. Hammad, Environ. Nanotechnol. Monit. Manag. **18**, 100672 (2022)
49. K. Li, P.Y. Dugas, E. Bourgeat-Lami, M. Lansalot, Polymer **106**, 249 (2016)